Modelling the flow of droplets of bio-pesticide on foliage

S. Veremieiev*[1], A. Brown[2], P.H. Gaskell[3], C.R. Glass[4], N. Kapur[5], and H.M. Thompson[5]

[1]School of Engineering, Technology and Maritime Operations, Liverpool John Moores University, Liverpool, L3 3AF, UK
[2]BASF Agricultural Specialities Ltd., Harwood Industrial Estate, Harwood Road, Littlehampton West Sussex, BN17 7AU, UK
[3]School of Engineering and Computing Sciences, Durham University, Durham, DH1 3LE, UK
[4]Food and Environment Research Agency, Sand Hutton, York, YO41 1LZ, UK
[5]School of Mechanical Engineering, University of Leeds, Leeds, LS2 9JT,UK

February 11, 2014

Abstract

The flow of droplets of bio-pesticide, liquid laden with entomapathogenic nematodes (EPNs), over foliage approximated as a planar substrate is investigated theoretically via a simple analytical model and computationally by solving a sub-set of the Navier-Stokes equations arising from application of the long-wave approximation. That the droplets of interest can be represented as a homogeneous liquid is established via complementary experiments revealing the presence of EPNs to have negligible influence on bio-pesticide droplet spray distributions pre-deposition. Both approaches are used to study key issues affecting the migration of droplets over substrates relevant to pesticide deposition processes, including the effect (i) of droplet size and flow inertia on droplet morphology and coverage and (ii) of adaxial (above the leaf) or abaxial (under the leaf) flow orientations. The computational results obtained when inertia is accounted for are generally found to compare well with those given by the simple analytical model – a droplet's velocity relaxes to its terminal value very quickly, at which point gravitational, viscous and hysteresis forces are in balance; substrate orientation is found to have only a minor influence on the extent of droplet migration.
Keywords: droplets, fluid-flow, experiments, analysis, computations, bio-pesticide.

1 Introduction

The migration of droplets residing on a substrate is ubiquitous throughout science and engineering and is crucial to several natural, engineering and manufacturing processes. Important examples are encountered in the deposition of coatings and inks, in enhanced oil recovery, the direct patterning of functional layers during microchip production and the cooling of electronic components, see for example Bear (1988); Gaskell *et al.* (2008); Anandan & Ramalingam (2008).

*Corresponding author: S.Veremieiev@ljmu.ac.uk

The motion of such droplets can be induced in several ways: electrostatically, Kim *et al.* (2002), via temperature or chemical gradients, Tseng *et al.* (2004), due to shearing from the movement of a surrounding fluid, usually air, Ding & Spelt (2008), and, of particular relevance here, by gravity, Le Grand *et al.* (2005); Schwartz *et al.* (2005), the environmental driver being the need to achieve more efficient and sustainable usage of pesticides. In addition, since legislation is limiting the use of chemically active pesticides for pest control in crops, the present focus is the study of droplet motion relevant to bio-pesticides involving entomapathogenic nematodes (EPNs) as components of an integrated pest management system, Matthews (2000).

Several previous experimental, analytical and computational studies of droplet motion over substrates provide important knowledge and information relevant to pesticide deposition on foliage, see for example the review of Yarin (2006) concerning the fundamental dynamics associated with droplet impact, splashing and spreading. Other experimental investigations include the distortion and pearling of gravity-driven droplets on an inclined plane, Podgorski *et al.* (2001); Le Grand *et al.* (2005), and more recently ones involving the movement of droplets due to shearing air flows, Fan *et al.* (2011), together with the impact and/or coalescence of deposited surface droplets, Kapur & Gaskell (2007); Castrejon-Pita *et al.* (2011). These are complemented by more applied experimental explorations which have focussed on key practical spreading indicators such as the evolution of droplet radii with time, droplet spread factors (ratio of final to initial cross-sectional area) and droplet evaporation times. Another important consideration, since agrochemical products typically contain between 1-10% of one or more surfactant, concerns the key role of adjuvants and the resultant effects on dynamic surface tension, which have also been investigated widely, Xu *et al.* (2011). Several researchers have quantified how the addition of adjuvants leads to larger spread factors and a reduction in evaporation time, enabling smaller droplets to be retained on difficult-to-wet foliage.

It is recognised that a better understanding of droplet migration over foliage via modelling can play an important role in achieving optimum pesticide usage by providing greater understanding of the key influences of droplet size, impact velocity, consituent parameters and foliage properties, Teske *et al.* (2011). Several useful models have already been developed to predict the motion of droplets on solid substrates, see for example Deegan (2000); Cachile *et al.* (2002), many of which simplify the governing equations for situations where flow inertia is deemed negligible. Recent studies have focussed on incorporating more complex physics into such flow models, such as the influence of surfactants, Chengara *et al.* (2007), humidity levels, Dunn *et al.* (2008), substrate thermal conductivity, Dunn *et al.* (2009), and have been highly successful in modelling 2-D and axisymmetric flow over homogeneous substrates.

In terms of obtaining complex three-dimensional numerical solutions to such free-surface flow problems, the significant computational challenges and resource requirements involved has led to very few results, based on solving the full Navier-Stokes equations, appearing in the literature to date. Those that do have employed, in the main, the topological flexibility of Finite Element (FE) methods coupled with Arbitrary Lagrangian-Eulerian (ALE) techniques for tracking free-surface locations. Examples include the study of free-surface flow with wetting lines by Baer *et al.* (2000) and simulations of injection moulding by Wang & Li (2010). The lattice Boltzmann method is also showing promise for simulating droplet flows and offers potentially significant advantages over FE-based methods in terms of topological flexibility and scalability for High Performance Computing applications; see the recent exploration of droplet impact and coalescence by Castrejon-Pita *et al.* (2011).

The above computational drawbacks in relation to solving free-surface flows in general, and droplet flows in particular, has motivated the development of a range of efficient numerical methods in the last decade or so based on simplifying the full Navier-Stokes equations via the long-wave approximation in situations where the fact that the characteristic film thickness is small compared to the characteristic in-plane length scale can be exploited. The additional simplifying assumption of negligible inertia enables the flows to be represented by either a single 4th

order non-linear degenerate partial differential equation for the film thickness or a coupled set of equations for the film thickness and pressure, albeit with formal restrictions to surface tension-dominated flows with small capillary number, Lee *et al.* (2009); Gaskell *et al.* (2010); Cowling *et al.* (2011). By employing a precursor film model to alleviate the singularity associated with the three-phase contact lines present, this so-called lubrication model, Oron *et al.* (1997), has been used successfully to investigate a variety of droplet flows at zero Reynolds number. Examples include flow over homogeneous substrates with, Schwartz *et al.* (2001), and without, Glass *et al.* (2010), evaporation, with surfactants, Schwartz *et al.* (2004) and for a non-Newtonian power-law liquid, Ahmed *et al.* (2013), over heterogeneous substrates with variable wettability, Schwartz & Eley (1998) and containing in addition micro-scale topographical features, Gaskell *et al.* (2004). A key challenge is achieving mesh independent solutions, Koh *et al.* (2009), and spreading rates quantitatively comparable with those observed experimentally, Gaskell *et al.* (2008).

Since the influence of inertia on free-surface flow can be important in terms of surface deformation and stability, lubrication-type models for continuous thin film flows at non-zero Reynolds number have appeared, see for example Veremieiev *et al.* (2010) who developed a depth-averaged approach, akin to the integral boundary layer equations first reported by Shkadov (1967, 1968), for exploring such problems. Related experiments, other than in the low Reynolds number regime, have lagged behind; however Puthenveettil *et al.* (2013) has recently addressed this issue and reported a comprehensive set of experimental results, data and visualisations, for the motion of water and mercury droplets on an inclined plane surface in, as they term it, the inertial regime. They derive an analytical expression for the dimensionless velocity of their drops, covering the Reynolds number range explored, and compare their dynamic contact angle data to models that have appeared in the literature.

The following section gives a brief description of an experimental study into the effect of adding EPNs and a commercial adjuvant on droplet size distribution in bio-pesticide sprays. In section 3 both an analytical model and one involving the numerical solution of a governing equation set based on application of the long-wave approximation, for droplet flow over an inclined planar substrate, are presented. The results provided in Section 4 consider the influence of droplet parameters, flow inertia and leaf orientation on droplet migration, with predictions compared against experimental data; conclusions are drawn in Section 5.

2 Experimental Measurement of Bio-Pesticide Droplet Size Distribution

Bio-pesticides utilise living organisms to kill pests, with the use of EPNs which attack pests by entering body openings and releasing bacteria that prevent pests from feeding becoming increasingly popular. Commercial bio-pesticides are prepared by mixing EPNs in a carrier solution and then mixing this with water and adjuvants before spraying onto leaves. In order to determine the influence of EPNs on droplet size distribution and hence if the droplets produced behave as if a homogeneous liquid, a series of experiments was carried out with water and different concentrations of a commercial adjuvant supplied by Becker Underwood. The commercial bio-pesticide, which includes 10% carrier material with the infective juvenile stage nematodes *Steinernema Feltiae*, was mixed with water and adjuvant to give a nematode concentration of 125000/L. Sprays were generated using a Teejet XR11005 nozzle at a pressure of 0.8 bar.

Spray size measurements were carried out using the Malvern Spraytec laser diffraction system, which is based on the principle that particles passing through a laser beam scatter light at an angle directly related to their size; the diffraction pattern is transformed into a particle size distribution using Lorenz-Mie theory for the scattering of electromagnetic radiation by spherical particles. Measurements were averaged over time and at three different locations A,

B and C of the spray, as indicated in Fig. 1.

The reported Volume Median Diameter (VMD) Dv0.5, is defined as the droplet diameter where half of the spray droplets have a smaller diameter. The experiments performed revealed both the carrier material and the EPNs to have a minor influence on the droplet size distribution of the spray when compared with the same for a water-adjuvant only control. Table 1 shows the influence of adjuvant concentration on the VMD of the spray. Low concentrations of adjuvant have little effect on the VMD; however, the latter increases significantly when the adjuvant concentration is increased to 0.3% and beyond. Since the EPNs represent a very small proportion of the total droplet volume, Lello *et al.* (1996), these findings are significant and sufficient to suggest that droplets of bio-pesticide can be suitably modelled by assuming them to be essentially a homogeneous liquid for droplets in flight and post deposition.

3 Droplet Flow Models

Two models have been formulated to investigate the problem of interest, namely droplet flow on planar substrate post-deposition: one results in analytical expressions for the terminal velocity and relaxation time of such droplets, based on a simple force balance argument; the other leads to a coupled governing partial differential equation set that is solved numerically and from which the associated predicted terminal velocity and relaxation times are extracted.

3.1 Analytical Formulation

Fig. 2a is a schematic of the side-view, at time T, of a liquid droplet of volume V_0, having initial velocity U_0, flowing down substrate inclined at an angle α to the horizontal, where the chosen Cartesian streamwise, X and normal, Z, coordinates are as indicated. The liquid is assumed to be incompressible and to have constant density, ρ, dynamic viscosity, μ, and surface tension, σ. The motion of the droplet is governed by competing gravitational, drag and hysteresis forces, and Newton's second law applied down the substrate yields:

$$\rho V_0 \frac{dU_c}{dT} = \rho g_0 V_0 \sin\alpha - F_{drag} - F_{hyst}, \tag{1}$$

where g_0 is the standard gravity constant, U_c is the droplet's velocity at any time, $F_{drag} = c_s \mu L_0 U_c$ is the viscous drag on the droplet, $L_0 = V_0^{1/3}$ is the characteristic size of the droplet, c_s is the dimensionless Stokes drag coefficient, $F_{hyst} = \sigma L_0 \Delta$ is the interfacial force due to contact angle hysteresis and Δ is the dimensionless hysteresis coefficient. F_{hyst} arises due to the heterogeneous nature of foliage, where Scanning Electron Microscopy reveals a large diversity of leaf micro-structures, Koch *et al.* (2009), that lead to significant local variations in wettability. Including such small-scale variations in substrate properties is currently not feasible, so the popular approach is to model them by specifying different substrate contact angles for advancing and receding contact line motion, Glass *et al.* (2010).

Inserting F_{drag} and F_{hyst}, as defined above, in equation (1) and integrating yields:

$$U_c = U_t \left(1 - e^{-T/\tau}\right) + U_0 e^{-T/\tau}, \tag{2}$$

with the droplet's terminal (asymptotic) velocity and relaxation time to terminal velocity given by:

$$U_t = \frac{\rho g_0 L_0^2 \sin\alpha - \sigma\Delta}{c_s \mu}, \tag{3}$$

and

$$\tau = \frac{\rho L_0^2}{c_s \mu}, \tag{4}$$

respectively. The minimum volume, V_0^{min}, of the smallest droplet that is able to move over the substrate is found by setting $U_t = 0$ in equation (3):

$$V_0^{min} = \left(\frac{\sigma \Delta}{\rho g_0 \sin \alpha} \right)^{3/2}. \tag{5}$$

Equations (3) and (5) are the same as relations (5.2) and (5.3) from Dussan (1985); equation (3) can also be expressed in dimensionless form as follows:

$$c_s \mathrm{Ca} = \mathrm{Bo} - \Delta, \tag{6}$$

where $\mathrm{Bo} = \rho g_0 L_0^2 \sin \alpha / \sigma$ is the Bond number, measuring the relative importance of the X-component of gravity to surface tension forces and $\mathrm{Ca} = \mu U_t / \sigma$ is the capillary number, measuring the relative importance of the viscous forces to surface tension forces. The Reynolds number, measuring the relative importance of inertial to viscous forces, is defined as $\mathrm{Re} = \rho U_t L_0 / \mu$.

Le Grand *et al.* (2005) reported experimentally obtained dimensionless hysteresis coefficient values, Δ^{exp}, close to the theoretical ones, Δ^{th}, obtained for $\mathrm{Ca} \ll 1$ and $\mathrm{Re} \ll 1$, see Dussan (1985), given by:

$$\Delta^{th} = \left(\frac{24}{\pi} \right)^{1/3} \frac{(\cos \theta_r - \cos \theta_a)(1 + \cos \theta_a)^{1/2}}{(2 + \cos \theta_a)^{1/3} (1 - \cos \theta_a)^{1/6}}, \tag{7}$$

where θ_a and θ_r are the advancing and receding contact angles made with the substrate, respectively, see Table 2. In the present study comparisons are also made of the experimental values for c_s, c_s^{exp} with the the theoretical ones from Dussan (1985):

$$c_s^{th} = \left(\frac{\partial \theta_a}{\partial \mathrm{Ca}} + \frac{\partial \theta_r}{\partial \mathrm{Ca}} \right) \frac{\sin^2 \theta_a}{2} \left(\frac{3\pi^2}{2 - 3 \cos \theta_a + \cos^3 \theta_a} \right)^{1/3}, \tag{8}$$

where $\partial \theta_a / \partial \mathrm{Ca}$ and $\partial \theta_r / \partial \mathrm{Ca}$ are inverse contact line capillary numbers that are characterised by the wetting dynamics; their values are taken from Figure 18 of Le Grand *et al.* (2005) for 47V10, 47V100 and 47V1000 liquids and for water from Puthenveettil *et al.* (2013). Other related data from Podgorski *et al.* (2001) and Kim *et al.* (2002*a*) are also provided in Table 2 for completeness. Δ^{th} is found to be 32% larger than its experimental counterpart, Δ^{exp}, from the work of Podgorski *et al.* (2001). For the Le Grand *et al.* (2005) case studies, Δ^{th}, is found to be up to 37% larger than Δ^{exp}, while c_s^{th} is 16% greater than the experimental estimate c_s^{exp}. With reference to the data of Puthenveettil *et al.* (2013), Δ^{th}, is within 1% of Δ^{exp}, while c_s^{th} is found to be 13% greater than the c_s^{exp} estimate.

Although the above comparison shows that this simple analytical model is a useful guide for steady droplet flows, as Bo (L_0) increases the experimental data of Podgorski *et al.* (2001) and Le Grand *et al.* (2005) shows that the linear relationship between Ca and Bo, predicted by equation (6), breaks down when cusps develop at the rear of a moving droplet. Such droplet distortions, which eventually lead to secondary, pearl droplets (Schwartz *et al.* (2005); Koh *et al.* (2009)), are able to be predicted via numerical solutions of the model described below.

3.2 Depth-Averaged Form (DAF): Numerical Formulation

Fig. 2b is a schematic of the three-dimensional droplet motion of interest. The Cartesian streamwise, X, spanwise, Y, and normal, Z, coordinate system adopted is as indicated, with the solution domain bounded from below by the surface, $Z = 0$, from above by the free surface, $Z = H(X, Y, T)$, upstream and downstream by the inflow, $X = 0$, and outflow, $X = L_p$, planes respectively and to the left and right by the side planes at $Y = 0$ and $Y = W_p$. The variable

H is *a priori* unknown and the laminar flow is described by the Navier-Stokes and continuity equations, namely:

$$\rho\left(\frac{\partial \boldsymbol{U}}{\partial T}+\boldsymbol{U}\cdot\nabla\boldsymbol{U}\right)=-\nabla P+\mu\nabla^2\boldsymbol{U}+\rho\boldsymbol{G}, \tag{9}$$

$$\nabla\cdot\boldsymbol{U}=0, \tag{10}$$

where $\boldsymbol{U}=(U,V,W)$ and P are the fluid velocity and pressure, respectively; $\boldsymbol{G}=g_0\left(\sin\alpha,0,-\cos\alpha\right)$ is the acceleration due to gravity.

Solving equations (9) and (10) subject to appropriate boundary conditions is extremely challenging and the associated computational resource requirements mean that such solutions are rare. The significant computational challenges of simulating droplet flows can be alleviated using the so-called long-wave approximation based on an assumption that the ratio $\varepsilon=H_0/L_0\ll 1$, where H_0 is the characteristic initial droplet height. Following Gaskell *et al.* (2004) all analyses are performed and results presented in terms of corresponding non-dimensional (lower case) variables, the key ones being:

$$(x,y)=\frac{(X,Y)}{L_0},\ (z,h)=\frac{(Z,H)}{H_0},\ t=\frac{TU_0}{L_0},\ p=\frac{L_0P}{\sigma\varepsilon},\ \left(u,v,\frac{w}{\varepsilon}\right)=\frac{(U,V,W)}{U_0}. \tag{11}$$

The resulting Depth-Averaged Form (DAF) of the governing continuity and Navier-Stokes equations, see Veremieiev *et al.* (2010) for the full details, retains the inertia terms:

$$\frac{\mathrm{Re}_0\mathrm{Ca}_0}{\varepsilon}\left[\frac{\partial\bar{u}}{\partial t}-\frac{\bar{u}}{5h}\frac{\partial h}{\partial t}+\frac{6}{5}\left(\bar{u}\frac{\partial\bar{u}}{\partial x}+\bar{v}\frac{\partial\bar{u}}{\partial y}\right)\right]=-\frac{\partial p}{\partial x}-\frac{3\mathrm{Ca}_0\bar{u}}{\varepsilon^3h^2}+\frac{\mathrm{Bo}}{\varepsilon}, \tag{12}$$

$$\frac{\mathrm{Re}_0\mathrm{Ca}_0}{\varepsilon}\left[\frac{\partial\bar{v}}{\partial t}-\frac{\bar{v}}{5h}\frac{\partial h}{\partial t}+\frac{6}{5}\left(\bar{u}\frac{\partial\bar{v}}{\partial x}+\bar{v}\frac{\partial\bar{v}}{\partial y}\right)\right]=-\frac{\partial p}{\partial y}-\frac{3\mathrm{Ca}_0\bar{v}}{\varepsilon^3h^2}, \tag{13}$$

$$\frac{\partial h}{\partial t}+\frac{\partial}{\partial x}\left(h\bar{u}\right)+\frac{\partial}{\partial y}\left(h\bar{v}\right)=0, \tag{14}$$

$$p=-\left(\frac{\partial^2h}{\partial x^2}+\frac{\partial^2h}{\partial y^2}\right)+\mathrm{Bo}\cot\alpha\left(h-z\right)-\Pi(h), \tag{15}$$

where $\mathrm{Ca}_0=\mu U_0/\sigma$ and $\mathrm{Re}_0=\rho U_0L_0/\mu$ are the capillary and Reynolds numbers based on the initial velocity U_0, the over-bar denotes depth-averaged components of velocity, namely:

$$\bar{u}=\frac{1}{h}\int_0^h u\,dz,\quad \bar{v}=\frac{1}{h}\int_0^h v\,dz. \tag{16}$$

In equation (15) a disjoining pressure, $\Pi(h)$, has been introduced to alleviate the singularity that would otherwise occur at the droplet's dynamic contact line, where θ is the liquid's dynamic contact angle with the substrate, h^* is the precursor film thickness and the constants n and m are exponents of the interaction potential, Schwartz & Eley (1998):

$$\Pi(h)=\frac{(n-1)\,(m-1)\,(1-\cos\theta)}{\varepsilon^2h^*\,(n-m)}\left[\left(\frac{h^*}{h}\right)^n-\left(\frac{h^*}{h}\right)^m\right]. \tag{17}$$

In the results reported subsequently, inertialess flows are modelled by setting the left hand sides of equations (12) and (13) to zero, while the effect of leaf heterogeneity is modelled in terms of its advancing (θ_a), receding (θ_r) and equilibrium (θ_e) contact angles, namely:

$$\theta=\begin{cases}\theta_a,\ \frac{\partial h}{\partial t}>0,\\ \theta_r,\ \frac{\partial h}{\partial t}<0,\\ \theta_e,\ \frac{\partial h}{\partial t}=0.\end{cases} \tag{18}$$

Equations (12) to (15) are solved subject to symmetry boundary conditions at the edges of the computational domain, namely:

$$\frac{\partial\left(\bar{u},\bar{v},p,h\right)}{\partial x}|_{x=0,l_p}=\frac{\partial\left(\bar{u},\bar{v},p,h\right)}{\partial y}|_{y=0,w_p}=0. \tag{19}$$

At the start of the motion, all droplets have centre of mass velocity U_0 and are assumed to be elliptic paraboloids defined by:

$$h\left(x,y,0\right)=\max\left[1-\frac{\left(x-x_0\right)^2+\left(y-y_0\right)^2}{r_0^2},h^*\right], \tag{20}$$

where x_0 and y_0 are the initial coordinates of the centre of mass of the droplet, while the velocity components are set to $\bar{u}\left(x,y,0\right)=2h^2$ and $\bar{v}\left(x,y,0\right)=0$. Using the relations for dimensionless volume, $1/\varepsilon=\pi r_0^2/2$, and contact angle of the paraboloid, $\tan\theta_e=2\varepsilon/r_0$, the in-plane dimensionless radius $r_0=\left(4/\pi\tan\theta_e\right)^{1/3}$ and long-wave ratio $\varepsilon=\left(\tan^2\theta_e/2\pi\right)^{1/3}$ are obtained. From the latter expression it follows that the long-wave approximation, $\varepsilon\ll 1$, is not applicable if θ_e is too large, although results suggest that it can remain valid outside of this formal range of applicability.

The above equations, subject to the attendant boundary conditions, are solved on a rectangular computational domain $(x,y)\in\Omega=(0,l_p)\times(0,w_p)$, subdivided using a staggered arrangement of unknowns, consisting of n_x and n_y regular cells in the x and y directions respectively. The unknown variables, thickness h, pressure p and velocity components $(\bar{u},\bar{v})$ are located at cell centres (i,j) and cell faces $(i+1/2,j)$, $(i,j+1/2)$, respectively. An automatic adaptive time-stepping procedure which utilises estimates of the local truncation error to optimise the size of the time steps and minimise computational cost is employed. At the solution stage of the temporal discretisation, the system of equations is solved using a customised multigrid strategy. The discretised equations are solved using a fixed number of Full Approximation Storage V-cycles on intermediate grid levels and up to 10 V-cycles on the first grid level so that residuals are reduced below a specified tolerance. Further details concerning the spatial and temporal discretisation schemes and the multigrid solution method are available in Veremieiev *et al.* (2010).

4 Results

The effect of droplet volume, inertia and substrate orientation on droplet migration over heterogeneous substrate are explored. Numerical results are obtained for an initial droplet speed $U_0=0.5$ m/s and when the physical parameters of the liquid are set to: $\rho=1000$ kg/m^3, $\sigma=0.0632$ N/m, $\mu=0.00142$ Pa $\cdot$ s, based on a 0.1% concentration adjuvant solution in water, with $\theta_e=45^\circ$, $\theta_a=50^\circ$, $\theta_r=40^\circ$, $h^*=0.01$, $m=2$, $n=3$, $l_p=20r_0$, $w_p=5r_0$, $x_0=5r_0$, $y_0=2.5r_0$, $n_x=512$, $n_y=128$.

4.1 Effect of Droplet Geometry and Inertia

Figures 3 and 4 show the effect of increasing Bo (increasing L_0) on the flow of different droplets down an inclinded plane ($\alpha=60^\circ$) without ($\mathrm{Re}_0=0$) and with inertia ($\mathrm{Re}_0\neq 0$) respectively. For flow without inertia the shape of the droplet footprint remains approximately circular. Figure 4 shows that the inclusion of inertia leads to an initial elongation of the droplet footprint before relaxation towards an asymptotic quasi-circular footprint at later times. For the droplet with the largest considered Bond number, Bo = 0.62 ($L_0=2.2$mm), there is a particularly large initial elongation which leads to a long tail; however this anyway subsequently relaxes towards a quasi-circular droplet footprint.

Figure 5 shows the effect of increasing droplet size on the evolution of the velocity of the centre of mass of the droplet, U_c, calculated via:

$$U_c = U_0 \frac{\int\int_{(x,y)\in(h>h^*)} \bar{u} h dx dy}{\int\int_{(x,y)\in(h>h^*)} h dx dy}. \tag{21}$$

Note that in Figures 5 and 8 the analytical curves (2) and (6) are obtained using the experimental values of $c_s^{exp} = 150$ and $\Delta^{exp} = 0.17$ from Le Grand *et al.* (2005) for the flow of 47V10 fluid, whose viscosity is the closest to that of the 0.1% concentration adjuvant solution in water. For the cases where inertia is neglected, the DAF predicts that U_c relaxes to the terminal velocity much more quickly than the simple analytical model predicts, while the inclusion of inertia increases the relaxation time significantly and reduces the terminal velocity. This is shown in greater detail in Tables 3 and 4, which compare DAF predictions of the terminal migration velocity, U_t, and droplet velocity relaxation time, τ, against the corresponding analytical predictions given by equations (3) and (4) respectively obtained for $c_s^{exp} = 150$ and $\Delta^{exp} = 0.17$.

For case with flow inertia, Table 4 shows that both U_t and τ increase monotonically with droplet size. The analytical and DAF predictions of the relaxation time, τ, for inertial flows are in excellent agreement in all cases. Agreement between the two predictions of U_t improves as droplet size increases and is reasonably good for the larger droplets. However, for the smallest droplet, Bo = 0.06 (L_0 = 0.6mm), the analysis predicts droplet pinning while the DAF predicts U_t = 2mm/s. This feature of the numerical solutions has been discussed earlier, see e.g. Koh *et al.* (2009), and arises from the need for a contact-line model that removes the singularity that arises at wetting lines. The use of a precursor file model means that, although increasing computational grid refinement near the wetting line would reduce U_t for the Bo = 0.06 droplet, it is not capable of predicting pinning for such small droplets. Table 3 shows that the corresponding predictions of U_t for inertialess flow are consistently larger than those for inertial flows, particularly for smaller droplets, and are much larger than those predicted by the analytical model. It also shows that ignoring inertia causes the droplets to relax to terminal velocity much more quickly than predicted either by the numerical solutions or by equation (3).

4.2 Effect of Substrate Orientation

Since droplets of pesticide solution can flow either on the upper, adaxial, or lower, abaxial, surfaces of foliage it is of interest to know how substrate orientation affects droplet motion. Figure 6 show the corresponding predictions of the droplet shapes and the velocity of their centre of mass with $\alpha = 120^\circ$ for comparison with Figure 4. It is clear that for these droplet sizes, which are representative of pesticide sprays, substrate orientation has very little effect on the evolution of the droplet shape. Figure 7 shows the effect of substrate orientation on the evolution of U_c for both inertial and inertialess droplet flows. For inertialess flow, abaxial orientation leads to slightly smaller terminal velocities for smaller droplets and slightly larger ones for larger droplets; while for inertial flows the abaxial orientation leads to sligthly larger terminal velocities for all droplet sizes.

Finally, Figure 8 studies the effect of substrate orientation and inertia on the relationship between Bo and Ca, which equation (6) predicts to be linear. The linear fit to the numerical predictions in Figure 8 give $c_s = 133$ and $\Delta = 0.09$ for $\mathrm{Re}_0 \neq 0$ and $\alpha = 60^\circ$; $c_s = 127$ and $\Delta = 0.03$ for $\mathrm{Re}_0 = 0$ and $\alpha = 60^\circ$ and $c_s = 132$ and $\Delta = 0.09$ for $\mathrm{Re}_0 \neq 0$ and $\alpha = 120^\circ$. For inertialess flow the gradient of the line-of-best-fit increases slightly for abaxial flows, whereas for inertial flow the lines are unaffected by substrate orientation and are in closer agreement with equation (6).

5 Conclusions

Since few previous studies have considered the dynamics of bio-pesticide-laden droplets on foliage, this work provides a number of important insights for the understanding of pesticide deposition. It has shown that the use of EPNs at practical concentrations does not affect the VMD of bio-pesticide sprays and the motion of the droplets formed can be modelled by neglecting the influence of the nematodes and assuming droplet homogeneneity.

The computational results obtained generally support the insights provided by equations (2)-(6), which include the effect of droplet parameters and leaf properties on (i) the minimum droplet size that will flow on foliage and (ii) the velocity and timescale of droplet motions, which determine their mobility and may influence the survivability of the nematodes. The computational results also demonstrate that, for realistic bio-pesticide-laden droplet sizes, the difference between adaxial or abaxial flows, for a given angle of inclination to the horizontal, is small. Comparison between the relatively simple analytical model and more complex three-dimensional computational solutions, shows the former is consistent with corresponding experimental data provided by Podgorski *et al.* (2001), Le Grand *et al.* (2005) and Puthenveettil *et al.* (2013), and can predict the relationship between droplet migration velocity, viscous, hysteresis and gravitational forces for gravity-driven flow reasonably well provided droplet contact lines are smooth.

This investigation, which to the authors' knowledge is the first to predict computationally the influence of flow inertia on three-dimensional droplet migration, shows inertia to have an important influence on both the timescale of relaxation to terminal conditions and the value of a droplet's terminal velocity. For flows without inertia, droplets relax to terminal conditions very quickly and droplet footprints remain approximately circular as droplet size increases. In contrast, allowing for inertia in the numerical predictions leads to initial droplet elongation which increases the relaxation time to terminal velocity significantly, in excellent agreement with theory. The inclusion of inertia also leads to DAF predictions of terminal droplet velocity that are consistent with the accompanying analysis, except for small droplets where the latter predicts droplet pinning while the wetting models employed in obtaining the corresponding DAF solutions result in a small, non-zero droplet velocity.

Acknowledgements

SV gratefully acknowledges funding for his Knowledge Transfer Secondment into the Food and Environment Research Agency from the UK's Engineering and Physical Sciences Research Council.

Tables

Table 1: Volume Median Diameter, $Dv0.5$ (μm), obtained experimentally for combinations of water, adjuvant and EPNs, as a function of adjuvant concentration, c.

Substance	$c = 0\%$	$c = 0.01\%$	$c = 0.03\%$	$c = 0.1\%$	$c = 0.3\%$
Water + adjuvant	273.3	275.1	269.4	330.5	352.9
Water + carrier material + adjuvant	285.9	276.1	297.3	329.2	360.8
Water + carrier material + EPNs + adjuvant	271.0	272.8	282.6	307.5	360.6

Table 2: Comparison between Δ^{exp} and c_s^{exp} (inferred from data presented in (a) Podgorski *et al.* (2001), (b) Kim *et al.* (2002*a*), (c) Le Grand *et al.* (2005), and (d) Puthenveettil *et al.* (2013)) with Δ^{th}, equation (7), and c_s^{th}, equation (8), respectively.

Liquid	ρ, kg/m^3	σ, N/m	μ, Pa $\cdot$ s	θ_a, $^\circ$	θ_r, $^\circ$	$\frac{\partial\theta_a}{\partial Ca}$	$\frac{\partial\theta_r}{\partial Ca}$	c_s^{th}	c_s^{exp}	Δ^{th}	Δ^{exp}
47V10[(a)]	$\approx$ 940	0.0205	0.00915	$\approx$50	42	–	–	–	156	0.22	0.16
Ethylene glycol[(b)]	1114	0.0484	0.0209	–	–	–	–	–	666	–	0.26
Glycerin +water[(b)]	1228	0.0641	0.0600	–	–	–	–	–	449	–	0.50
Glycerin[(b)]	1260	0.063	0.95	–	–	–	–	–	736	–	0.29
47V10[(c)]	936	0.0201	0.0100	50.5	45.5	49	76	164	150	0.14	0.17
47V100[(c)]	964	0.0209	0.1037	52.9	42.7	44	53	128	109	0.28	0.20
47V1000[(c)]	970	0.0211	1.035	58.1	46.8	23	40	86	89	0.32	0.22
Water[(d)]	997	0.0720	0.000891	108.8	73.4	59	108	161	142	0.79	0.80

Table 3: Effect of Bo (L_0) on terminal (asymptotic) velocity and relaxation time for DAF ($\mathrm{Re}_0 = 0$) and $\alpha = 60^\circ$.

L_0, mm	Bo	τ, ms	τ^{th}, ms	U_t, mm/s	U_t^{th}, mm/s	Ca, 10^{-3}	Re
0.6	0.06	0.1	2.0	16	0	0.4	7
1.3	0.21	0.2	7.4	63	13	1.4	56
1.6	0.34	0.2	11.8	97	50	2.2	108
1.9	0.49	0.3	17.2	148	95	3.3	200
2.2	0.62	0.3	21.8	219	135	4.9	332

Table 4: Effect of Bo (L_0) on asymptotic velocity and relaxation time for DAF ($\mathrm{Re}_0 \neq 0$) and $\alpha = 60°$.

L_0, mm	Bo	τ, ms	τ^{th}, ms	U_t, mm/s	U_t^{th}, mm/s	Ca, 10^{-3}	Re
0.6	0.06	2.6	2.0	2	0	0.1	1
1.3	0.21	8.5	7.4	20	13	0.4	17
1.6	0.34	12.4	11.8	83	50	1.9	93
1.9	0.49	17.1	17.2	135	95	3.0	182
2.2	0.62	21.2	21.8	181	135	4.1	275

Table 5: Effect of Bo (L_0) on asymptotic velocity and relaxation time for DAF ($\mathrm{Re}_0 \neq 0$) and $\alpha = 120°$.

L_0, mm	Bo	τ, ms	τ^{th}, ms	U_t, mm/s	U_t^{th}, mm/s	Ca, 10^{-3}	Re
0.6	0.06	2.6	2.0	3	0	0.1	1
1.3	0.21	8.6	7.4	20	13	0.4	18
1.6	0.34	12.8	11.8	85	50	1.9	95
1.9	0.49	17.7	17.2	139	95	3.1	187
2.2	0.62	22.2	21.8	182	135	4.1	277

Figures

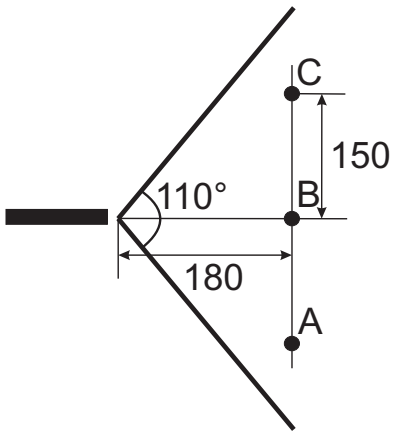

Figure 1: Schematic diagram of the Malvern Spraytec system: measurements are carried out and averaged over the points A. B and C. Dimensions are in mm.

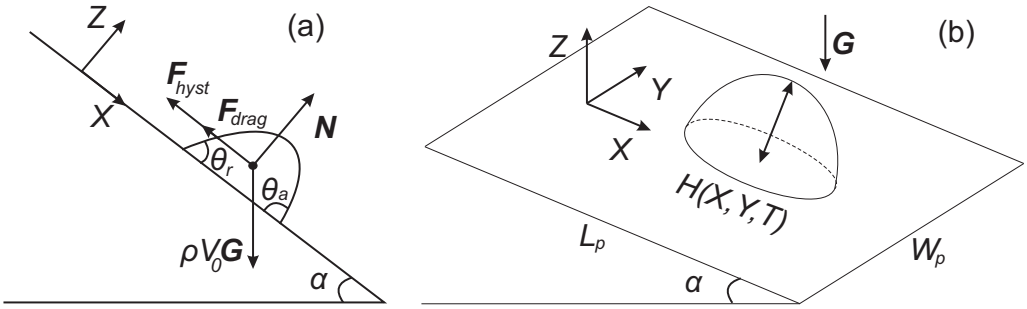

Figure 2: Schematic diagram of (a) the forces acting on a droplet migrating over an inclined planar substrate, shown in cross-section (b) three-dimensional droplet flow over an inclined planar substrate.

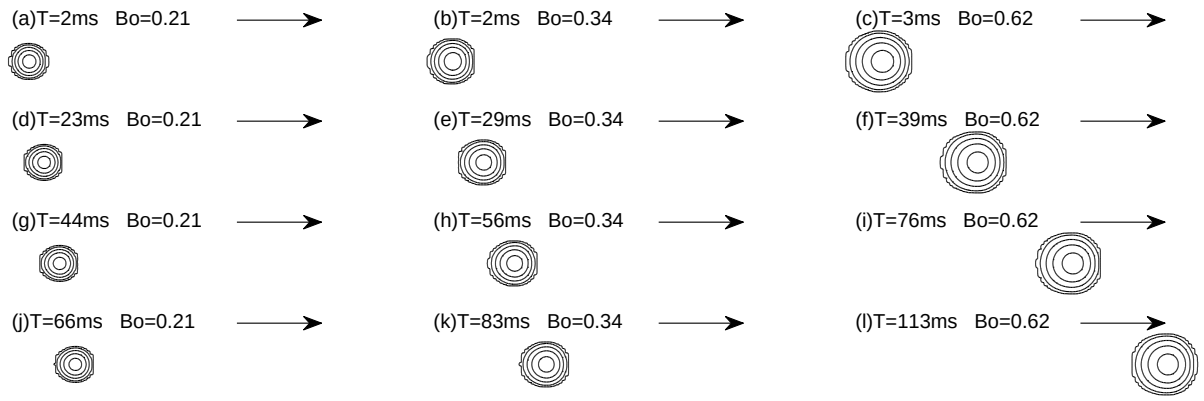

Figure 3: Droplet motion, from left to right, down an inclined planar surface viewed at various times showing the effect of Bo (L_0). DAF ($\mathrm{Re}_0 = 0$) solutions obtained for $\alpha = 60°$.

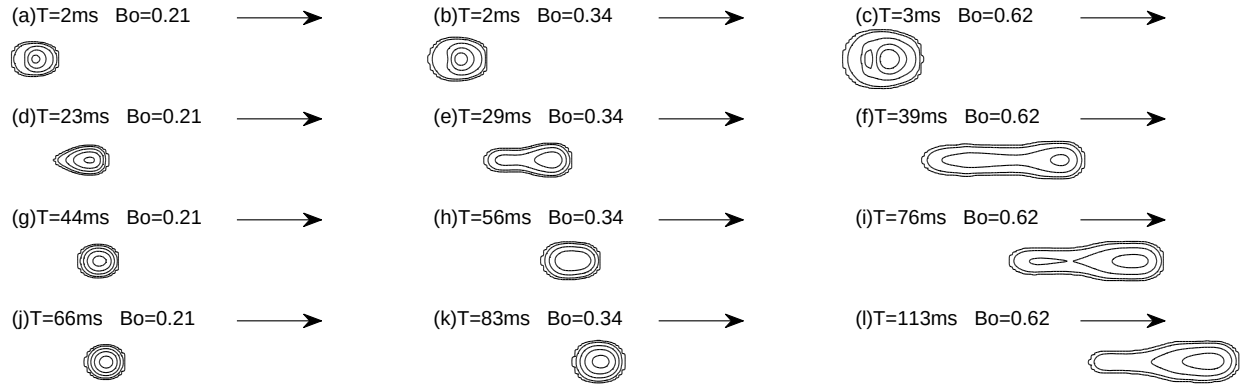

Figure 4: Droplet motion, from left to right, down an inclined planar surface viewed at various times showing the effect of Bo (L_0). DAF ($\mathrm{Re}_0 \neq 0$) solutions obtained for $\alpha = 60°$.

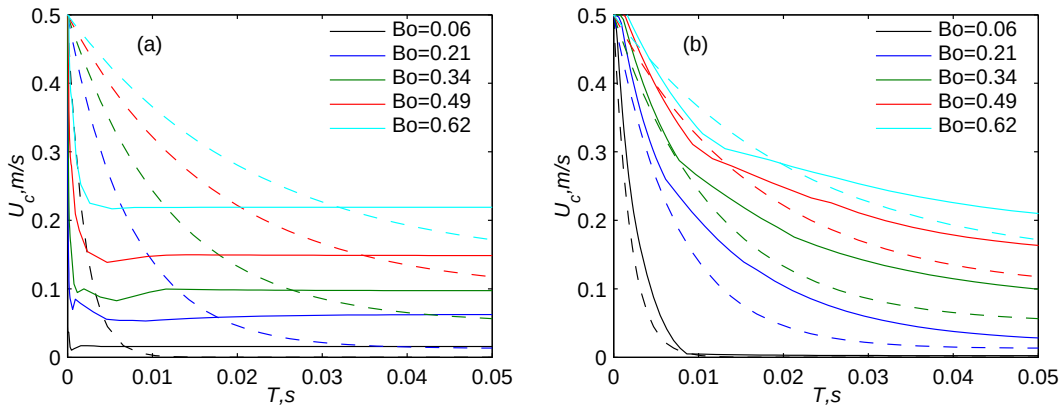

Figure 5: Effect of Bo (L_0) on the velocity of the centre of mass of drops flowing over an inclined plane with $\alpha = 60°$: (a) $\mathrm{Re}_0 = 0$; (b) $\mathrm{Re}_0 \neq 0$. Comparison of numerical predictions (solid lines) for 0.1% concentration PDS1038D solution in water with corresponding analytical values (dashed lines), equation (2), with c_s and Δ taken from experiment of Le Grand *et al.* (2005) for the flow of 47V10 fluid.

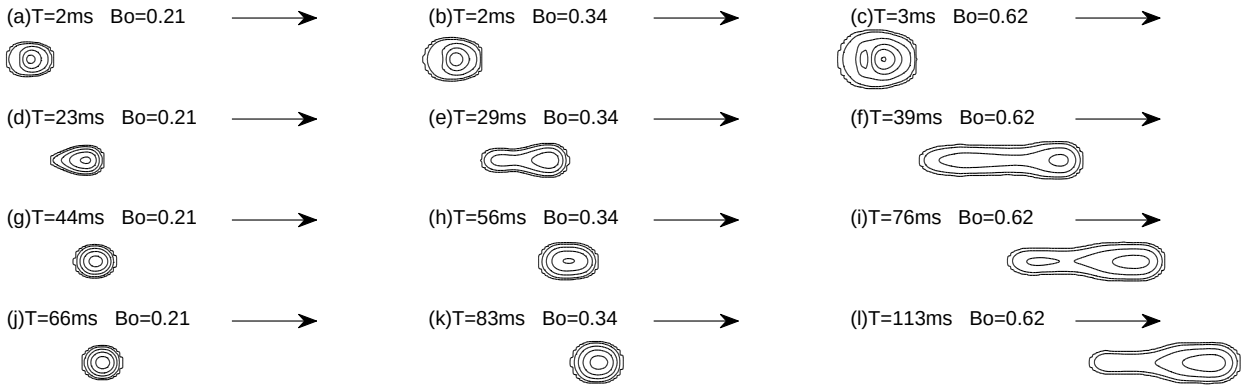

Figure 6: Droplet motion, from left to right, down an inclined planar surface viewed at various times showing the effect of Bo (L_0). DAF ($\mathrm{Re}_0 \neq 0$) solutions obtained for $\alpha = 120°$.

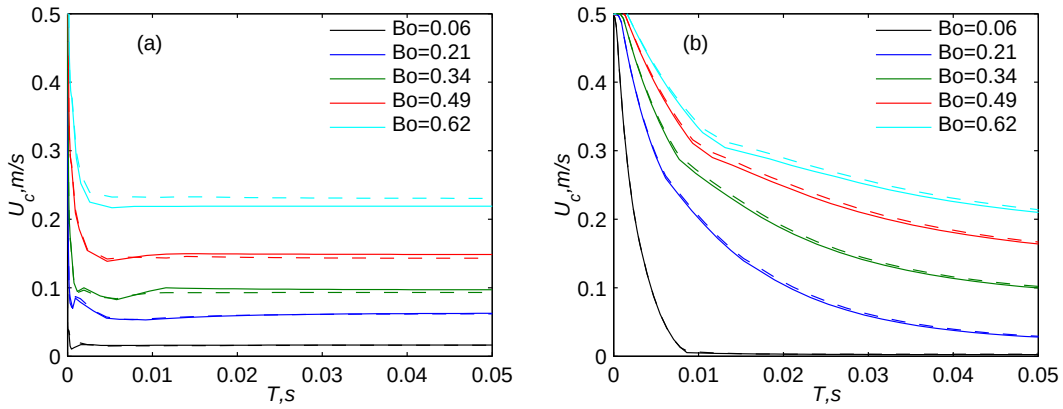

Figure 7: Effect of Bo (L_0) on the velocity of the centre of mass of drops flowing over a plane inclined at two different angles (adaxial for $\alpha = 60°$, solid lines vs. abaxial for $\alpha = 120°$, dashed lines), DAF: (a) $\mathrm{Re}_0 = 0$; (b) ($\mathrm{Re}_0 \neq 0$).

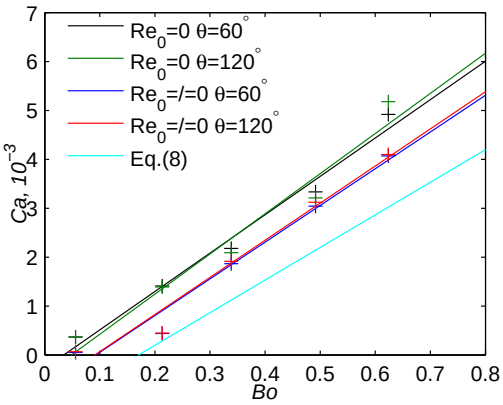

Figure 8: Ca vs. Bo: comparison of linear fits to DAF predictions for 0.1% concentration PDS1038D solution in water with the corresponding analytical values, equation (6), with c_s and Δ taken from the experiment of Le Grand *et al.* (2005) for the flow of 47V10 fluid.

References

Ahmed, G., Sellier, M., Lee, Y.C., Jermy, M. & Taylor, M. 2013 Modeling the spreading and sliding of power-law droplets. *Colloid Surfaces A Physicochem. Eng. Aspects* **432**, 2–7.

Anandan, S.S. & Ramalingam, V. 2008 Thermal management of electronics: A review of literature. *Thermal Science* **12** (2), 5–26.

Baer, T.A., Cairncross, R.A., Schunk, P.R., Rao, R.R. & Sackinger, P.A. 2000 A finite element method for free surface flows of incompressible fluids in three dimensions. Part II. Dynamic wetting lines. *Int. J. Num. Meth. Fl.* **33** (3), 405–427.

Bear, J. 1988 *Dynamics of fluids in porous media*. Dover books.

Cachile, M., Bénichou, O., Poulard, C. & Cazabat, A.M. 2002 Evaporating droplets. *Langmuir* **18** (21), 8070–8078.

Castrejon-Pita, J.R., Betton, E.S., Kubiak, K.J., Wilson, M.C.T. & Hutchings, I.M. 2011 The dynamics of the impact and coalescence of droplets on a solid surface. *Biomicrofluidics* **5** (1).

Chengara, A., Nikolov, A.D. & Wasan, D.T. 2007 Spreading of a water drop triggered by the surface tension gradient created by the localized addition of a surfactant. *Ind. Eng. Chem. Res.* **46** (10), 2987–2995.

Cowling, N.P., Gaskell, P.H., Lee, Y.C. & Thompson, H.M. 2011 Towards the efficient numerical solution of three-dimensional thin film flows on real surfaces: an evaluation of finite-difference-based schemes. *Proc. I. Mech. E. part C, J. Mech. Sci.* **225** (C8), 1886–1902.

Deegan, R.D. 2000 Pattern formation in drying drops. *Phys. Rev. E* **61** (1), 475–485.

Ding, H. & Spelt, P.D.M. 2008 Onset of motion of a three-dimensional droplet on a wall in shear flow at moderate reynolds numbers. *J. Fluid Mech.* **599**, 341–362.

Dunn, G.J., Wilson, S.K., Duffy, B.R., David, S. & Sefiane, K. 2008 A mathematical model for the evaporation of a thin sessile liquid droplet: Comparison between experiment and theory. *Colloid Surfaces A Physicochem. Eng. Aspects* **323** (1-3), 50–55.

Dunn, G.J., Wilson, S.K., Duffy, B.R., David, S. & Sefiane, K. 2009 The strong influence of substrate conductivity on droplet evaporation. *J. Fluid Mech.* **623**, 329–351.

Dussan, E.B. 1985 On the ability of drops or bubbles to stick to non-horizontal surfaces of solids. part 2. small drops or bubbles having contact angles of arbitrary size. *J. Fluid Mech.* **151**, 1–20.

Fan, J., Wilson, M.C.T. & Kapur, N. 2011 Displacement of liquid droplets on a surface by a shearing air flow. *J. Colloid Interf. Sci.* **356** (1), 286–292.

Gaskell, P.H., Jimack, P.K., Koh, Y.Y. & Thompson, H.M. 2008 Development and application of a parallel multigrid solver for the simulation of spreading droplets. *Int. J. Num. Meth. Fl.* **56** (8), 979–989.

Gaskell, P.H., Jimack, P.K., Sellier, M. & Thompson, H.A. 2004 Efficient and accurate time adaptive multigrid simulations of droplet spreading. *Int. J. Num. Meth. Fl.* **45** (11), 1161–1186.

Gaskell, P.H., Lee, Y.C. & Thompson, H.M. 2010 Thin film flow over and around surface topography: a general solver for the long-wave approximation and related equations. *CMES-Comp. Model. Eng. Sci.* **62** (1), 77–112.

Glass, C.R., Walters, K.F.A., Gaskell, P.H., Lee, Y.C., Thompson, H.M., Emerson, D.R. & Gu, X.J. 2010 Recent advances in computational fluid dynamics relevant to the modelling of pesticide flow on leaf surfaces. *Pest Manag. Sci.* **66** (1), 2–9.

Kapur, N. & Gaskell, P.H. 2007 Morphology and dynamics of droplet coalescence on a surface. *Phys. Rev. E* **75** (5), 056315.

Kim, H.Y., Lee, H.J. & Kang, B.H. 2002*a* Sliding of liquid drops down an inclined solid surface. *J. Colloid Interf. Sci.* **247** (2), 372–380.

Kim, J., Shen, W.J., Latorre, L. & Kim, C.J. 2002 A micromechanical switch with electrostatically driven liquid-metal droplet. *Sensors Actuat. A-Phys.* **97-8**, 672–679.

Koch, K., Bhushan, B. & Barthlott, W. 2009 Multifunctional surface structures of plants: An inspiration for biomimetics. *Prog. Mater. Sci.* **54** (2), 137–178.

Koh, Y.Y., Lee, Y.C., Gaskell, P.H., Jimack, P.K. & Thompson, H.M. 2009 Droplet migration: Quantitative comparisons with experiment. *Eur. Phys. J. Spec. Top.* **166**, 117–120.

Le Grand, N., Daerr, A. & Limat, L. 2005 Shape and motion of drops sliding down an inclined plane. *J. Fluid Mech.* **541**, 293–315.

Lee, Y.C., Thompson, H.M. & Gaskell, P.H. 2009 FILMPAR: A parallel algorithm designed for the efficient and accurate computation of thin film flow on functional surfaces containing micro-structure. *Comput. Phys. Commun.* **180** (12), 2634–2649.

Lello, E.R., Patel, M.N., Matthews, G.A. & Wright, D.J. 1996 Application technology for entomopathogenic nematodes against foliar pests. *Crop Protection* **15** (6), 567–574.

Matthews, G.A. 2000 *Pesticide Application Methods*, 3rd edn. Oxford: Wiley-Blackwell.

Oron, A., Davis, S.H. & Bankoff, S.G. 1997 Long-scale evolution of thin liquid films. *Rev. Mod. Phys.* **69** (3), 931–980.

Podgorski, T., Flesselles, J.M. & Limat, L. 2001 Corners, cusps, and pearls in running drops. *Phys. Rev. Lett.* **8703** (3).

Puthenveettil, B.A., Senthilkumar, V.K. & Hopfinger, E.J. 2013 Motion of drops on inclined surfaces in the inertial regime. *J. Fluid Mech.* **726**, 26–61.

Schwartz, L.W. & Eley, R.R. 1998 Simulation of droplet motion on low-energy and heterogeneous surfaces. *J. Colloid Interf. Sci.* **202** (1), 173–188.

Schwartz, L.W., Roux, D. & Cooper-White, J.J. 2005 On the shapes of droplets that are sliding on a vertical wall. *Phys. D Nonlinear Phenom.* **209** (1-4), 236–244.

Schwartz, L.W., Roy, R.V., Eley, R.R. & Petrash, S. 2001 Dewetting patterns in a drying liquid film. *J. Colloid Interf. Sci.* **234** (2), 363–374.

Schwartz, L.W., Roy, R.V., Eley, R.R. & Princen, H.M. 2004 Surfactant-driven motion and splitting of droplets on a substrate. *J. Eng. Math.* **50** (2-3), 157–175.

Shkadov, V.Y. 1967 Wave flow regimes of a thin layer of viscous fluid subject to gravity. *Izv. Akad. Nauk SSSR Fluid Dynamics* **2** (1), 29–34.

Shkadov, V.Y. 1968 Wave-flow theory for a thin viscous liquid layer. *Izv. Akad. Nauk SSSR Fluid Dynamics* **3** (2), 12–15.

Teske, M.E., Thistle, H.W., Schou, W.C., Miller, P.C.H., Strager, J.M., Richardson, B., Ellis, M.C.B., Barry, J.W., Twardus, D.B. & Thompson, D.G. 2011 A review of computer models for pesticide deposition prediction. *T. ASABE* **54** (3), 789–801.

Tseng, Y.T., Tseng, F.G., Chen, Y.F. & Cheng, C.C. 2004 Fundamental studies on micro-droplet movement by marangoni and capillary effects. *Sensors Actuat. A-Phys.* **114** (2-3), 292–301.

Veremieiev, S., Thompson, H.M., Lee, Y.C. & Gaskell, P.H. 2010 Inertial thin film flow on planar surfaces featuring topography. *Comput. Fluids* **39** (3), 431–450.

Wang, X.P. & Li, X.K. 2010 Numerical simulation of three dimensional non-Newtonian free surface flows in injection molding using ALE finite element method. *Finite Elem. Anal. Des.* **46** (7), 551–562.

Xu, L., Zhu, H., Ozkan, H.E., Bagley, W.E. & Krause, C.R. 2011 Droplet evaporation and spread on waxy and hairy leaves associated with type and concentration of adjuvants. *Pest Manag. Sci.* **67** (7), 842–851.

Yarin, A.L. 2006 Drop impact dynamics: Splashing, spreading, receding, bouncing. *Annu. Rev. Fluid Mech.* **38**, 159–192.